JOURNAL OF GUIDANCE, CONTROL, AND DYNAMICS
Vol. 24, No. 3, May–June 2001

Modeling and Simulation of Flexible Flight Vehicles

David K. Schmidt*
University of Colorado at Colorado Springs, Colorado Springs, Colorado 80918
and
David L. Raney†
NASA Langley Research Center, Hampton, Virginia 23681

The effects of flexibility on the flight dynamics of large aircraft have been shown to be quite significant, especially as the frequencies of the elastic modes become lower and approach those of the rigid-body modes. The handling characteristics of such vehicles are altered significantly from those of a rigid vehicle, and the design of the flight-control system may become drastically more complex. Consequently, the need to model accurately the dynamics of such vehicles, and to develop valid simulations, is becoming particularly acute. The theoretical development of a generic flexible-aircraft model is reviewed. This modeling technique allows for the flexible degrees of freedom to be added to an existing simulation model of the vehicle's rigid-body dynamics. The data necessary for modeling a specific vehicle include aerodynamic stability derivatives, aerodynamic influence coefficients, elastic mode shapes, modal frequencies and damping, and generalized masses. Two case studies are presented, both involving the development of motion-based simulations in NASA Langley Research Center's simulation facility. The first example investigates an aircraft similar in geometry to the B-1, whereas the second investigates a large highspeed commercial transport. The dynamic responses (time and frequency domain) for these vehicles are presented, along with the evaluations of the effects of dynamic aeroelasticity on their handling characteristics. The vehicle responses are critical to evaluating hardware and software requirements for simulation fidelity, for example, visual and motion cues. Finally, a brief assessment of the effects of limitations of the simulation facility is presented. Limitations considered include digital time delay, motion hardware bandwidth, and motion washout logic.

Introduction

THE effects of flexibility on the flight dynamics of aircraft have been shown to be quite significant, especially as the frequencies of the elastic modes become lower and approach those of the rigid-body modes. The handling characteristics of such vehicles are altered significantly from those of a rigid vehicle,[1] and the design of the flight-control system may become drastically more complex.[2,3] Consequently, the need to model accurately the dynamics of such vehicles, and to develop valid simulations, is becoming particularly acute.

Shown in Table 1, for example, are the lowest frequencies of the structural vibration modes for several flight vehicles. These data show that these frequencies can be lower than 3 Hz, and in some advanced supersonic-transport configurations (SCR in Table 1), the frequencies are as low as 1 Hz. Some are well within the bandwidth of the pilot and primary flight-control system, and others may certainly be excited by turbulence.

In this paper the theoretical development of a dynamic model for a generic flexible vehicle is reviewed. The model structure discussed is appropriate for any flexible atmospheric flight vehicle. Furthermore, this modeling technique allows for the flexible degrees of freedom to be added to an existing simulation based on a rigid-body model, a situation that can frequently occur.

Simulation results are then presented for two similar high-speed vehicles used in motion-based simulations performed in NASA Langley Research Center's simulation facility. Examples are presented of the dynamic responses (time and frequency domain) for these elastic vehicles. These responses are critical to evaluating hardware and software requirements for simulation fidelity, for example, in terms of visual and motion cues. Furthermore, a brief assessment of the effects of limitations due to the simulation hardware and software is presented. Limitations considered include digital time delay, motion hardware bandwidth and displacement limits, and motion washout logic.

Presented as Paper 98-4359 at the AIAA Modeling and Simulation Technologies Conference, Boston, MA, 10–12 August 1998; received 21 December 1998; revision received 15 August 2000; accepted for publication 30 August 2000. Copyright © 2000 by David K. Schmidt and David L. Raney. Published by the American Institute of Aeronautics and Astronautics, Inc., with permission.

*Professor and Director, Flight Dynamics and Control Laboratory. Fellow AIAA.
†Aerospace Engineer, Dynamics and Control Branch. Member AIAA.

Background

Of particular interest here are real-time, manned flight simulations, which may be motion based. Frequently a six-degree-of-freedom (DOF) simulation of the rigid vehicle has been developed, or the information required, for example, aerodynamic data, to perform such a simulation is available. One key issue then is how to develop the flexible-vehicle simulation by extending an existing rigid-body simulation.

The information/data that will be required include the aerodynamic data for the rigid vehicle, aerodynamic influence coefficients for the elastic deflections, in vacuo vibration frequencies and modes shapes for the structure, vehicle mass and inertias, and generalized masses for the elastic modes.

Finally, the vehicles for which elastic effects may be significant are of particular interest, for practical reasons. Therefore, the focus is on large, high-performance vehicles. Such vehicles usually have low elastic mode frequencies, approaching those of the rigid-body modes, and this situation is the most acute.

Modeling the Flexible Vehicle

A finite element analysis and perhaps ground vibration tests are assumed to have been performed, such that a modal description of the structure is available. That is, if the elastic deformation at a position (x, y, z) on the structure is denoted as $\boldsymbol{d}$, then it may be written as

$$\boldsymbol{d} = \sum_{i=1}^{\infty} \phi_i(x, y, z)\eta_i \tag{1}$$

where η_i is a generalized coordinate of the structure and $\phi_i(x, y, z)$ is a mode shape, or eigenfunction, associated with the generalized coordinate. Of course, a finite number of modes must be used, so that the model always is based on a truncated-mode description.

The selection of which modes to use is critical. However, basically one must select modes that can be excited and can contribute

Table 1 Examples of lowest structural vibration frequencies

Aircraft	Frequency, rad/s
B-1	13
Concorde	13+
C-5A	11
National Aerospace Plane	~18
SCR designs	~6.5

[a]Trends in elastic frequencies.

to important vehicle responses, such as cockpit accelerations. One must also include modes than may significantly couple with the rigid-body DOF. All of these factors usually imply using two to four of the lowest frequency modes per axis, depending on their mode shapes.

The equations of motion are developed with the use of a special body-referenced axis, the axis referred to by Milne[4] as the mean axis. This axis is the coordinate frame with respect to which the elastic deformations contribute no translational or rotational momentum. For the mean axis, the following relations hold:

$$\int_V \frac{\delta \boldsymbol{p}}{\delta t}\rho\,\mathrm{d}V = \int_V \boldsymbol{p} \times \frac{\delta \boldsymbol{p}}{\delta t}\rho\,\mathrm{d}V = 0$$

where an infinitesimal volume of the vehicle $\mathrm{d}V$ has location $\boldsymbol{p}$ with respect to the instantaneous c.m. of the vehicle. All of the equations of motion are derived using this body-referenced (mean) axis, and all forces, moments, and inertias must be resolved into components along and about the three directions, that is, x, y, and z of this axis.

Now let $\boldsymbol{p} = \boldsymbol{s} + \boldsymbol{d}$, where $\boldsymbol{s}$ is the position of $\mathrm{d}V$ with no elastic structural deformation and $\boldsymbol{d}(x, y, z)$ is the displacement of $\mathrm{d}V$ due to elastic deformation. When the modal representation for the elastic deformation $\boldsymbol{d}$ is used, the practical mean axes constraints may be used to determine the orientation of the mean axis if a modal representation of the structure is available for example, from a finite element analysis:

$$\sum_{i=1}^{\infty} \frac{\mathrm{d}\eta_i}{\mathrm{d}t}\int_V \phi_i \rho\,\mathrm{d}V = \sum_{i=1}^{\infty} \frac{\mathrm{d}\eta_i}{\mathrm{d}t}\int_V \boldsymbol{s} \times \phi_i \rho\,\mathrm{d}V = 0$$

Now let the inertial position of the instantaneous c.m. be R_0, the angular velocity of the vehicle-fixed (mean) axis relative to the inertial frame be $\boldsymbol{\omega}$, the total vehicle mass be M, and the vehicle's inertia tensor be I. (It is assumed that the inertia tensor remains constant, in spite of elastic deformations.) With the mean axis as defined, it can be shown[5] that the vehicle's kinetic energy can be expressed as follows:

$$T = \frac{1}{2}M\frac{\mathrm{d}\boldsymbol{R}_0^T}{\mathrm{d}t}\frac{\mathrm{d}\boldsymbol{R}_0}{\mathrm{d}t} + \frac{1}{2}\boldsymbol{\omega}^T[I]\boldsymbol{\omega} + \frac{1}{2}\int_V \frac{\partial \boldsymbol{p}^T}{\partial t}\frac{\partial \boldsymbol{p}}{\partial t}\rho\,\mathrm{d}V$$

Also, with the understanding that the first mass moment about the c.m. is zero, the gravitational potential energy can be shown to be

$$U_g = -\int_V (\boldsymbol{R}_0 + \boldsymbol{p})\cdot \boldsymbol{g}\rho\,\mathrm{d}V = -\boldsymbol{R}_0 \cdot \boldsymbol{g}\int_V \rho\,\mathrm{d}V - \boldsymbol{g}\cdot\int_V \boldsymbol{p}\rho\,\mathrm{d}V$$
$$= -\boldsymbol{R}_0 \cdot \boldsymbol{g}M \qquad (2)$$

where $\boldsymbol{g}$ is the gravitational acceleration vector. When the generalized mass of the ith mode is defined as

$$M_i = \int_V \phi_i \cdot \phi_i \rho\,\mathrm{d}V$$

the kinetic energy becomes

$$T = \frac{1}{2}M\frac{\mathrm{d}\boldsymbol{R}_0^T}{\mathrm{d}t}\frac{\mathrm{d}\boldsymbol{R}_0}{\mathrm{d}t} + \frac{1}{2}\boldsymbol{\omega}^T[I]\boldsymbol{\omega} + \frac{1}{2}\sum_{i=1}^{\infty} M_i\dot{\eta}_i^2 \qquad (3)$$

When the origin of the body-referenced (mean) axes is taken to be at the c.m., let

$$\boldsymbol{R}_0 = x\hat{i} + y\hat{j} + z\hat{k}$$

and

$$\frac{\mathrm{d}R_0}{\mathrm{d}t} = \left.\frac{\mathrm{d}R_0}{\mathrm{d}t}\right|_{\text{InertialAxis}} = \left.\frac{\partial R_0}{\partial t}\right|_{\text{BodyAxis}} + \boldsymbol{\omega} \times R_0 \equiv U\hat{i} + V\hat{j} + W\hat{k}$$

This relation defines the inertial velocity components U, V, and W. The three unit vectors are coincident with the orthogonal directions, that is, x, y, and z, of the body-referenced (mean) axis, which of course is not inertial.

Similarly, define the three components of the angular velocity resolved in the body-fixed axis by the relation

$$\boldsymbol{\omega} = p\hat{i} + q\hat{j} + r\hat{k}$$

where these components are related to the rates of change of the Euler angles by the usual relationships, or

$$p = \dot{\phi} - \dot{\psi}\sin\theta, \qquad q = \dot{\psi}\cos\theta\sin\phi + \dot{\theta}\cos\phi$$
$$r = \dot{\psi}\cos\theta\cos\phi - \dot{\theta}\sin\phi$$

Application of Lagrange's equation to the energy terms just defined [Eqs. (2) and (3)], leads to the following $6 + n$ elastic airplane equations of motion, where n is the number of elastic modes modeled:

$$M[\dot{U} - rV + qW + g\sin\theta] = Q_x$$

$$M[\dot{V} - pW + rU - g\sin\phi\cos\theta] = Q_y$$

$$M[\dot{W} - qU + pV - g\cos\phi\cos\theta] = Q_z$$

$$I_{xx}\dot{p} - (I_{xy}\dot{q} + I_{xz}\dot{r}) + (I_{zz} - I_{yy})qr + (I_{xy}r - I_{xz}q)p + (r^2 - q^2)I_{yz} = Q_{\phi_B}$$

$$I_{yy}\dot{q} - (I_{xy}\dot{p} + I_{yz}\dot{r}) + (I_{xx} - I_{zz})pr + (I_{yz}p - I_{xy}r)q + (p^2 - r^2)I_{xz} = Q_{\psi_B}$$

$$I_{zz}\dot{r} - (I_{xz}\dot{p} + I_{yz}\dot{q}) + (I_{yy} - I_{xx})pq + (I_{xz}q - I_{yz}p)r + (q^2 - p^2)I_{xy} = Q_{\psi_B}$$

$$\ddot{\eta}_i + 2\zeta_i\omega_i\dot{\eta}_i + \omega_i^2\eta_i = Q_{\eta i}/M_i \qquad i = 1, 2, 3, \ldots, n$$

where $Q_{(\cdot)}$ are the generalized forces acting on the system, due to aerodynamic and propulsive effects. Furthermore, ζ_i and ω_i are the damping and in vacuo vibration frequency of structural mode i, respectively.

Now define the total aerodynamic and propulsive forces and moments, resolved into components in the mean axes as

$$\boldsymbol{F} = \boldsymbol{X}\hat{i} + \boldsymbol{Y}\hat{j} + \boldsymbol{Z}\hat{k}, \qquad \boldsymbol{M} = \boldsymbol{L}\hat{i} + \boldsymbol{M}\hat{i} + \boldsymbol{N}\hat{k}$$

where

$$\boldsymbol{X} = L\sin\alpha - D\cos\alpha\cos\beta + S\cos\alpha\sin\beta + T_x$$

$$\boldsymbol{Y} = -D\sin\beta - S\cos\beta + T_y$$

$$\boldsymbol{Z} = -L\cos\alpha - D\sin\alpha\cos\beta + S\sin\alpha\sin\beta + T_z$$

where L is lift, D drag, S lateral force (aero), $\boldsymbol{L}$ rolling moment, $\boldsymbol{M}$ pitching moment, $\boldsymbol{N}$ yawing moment, and $T_{(\cdot)}$ the appropriate

component of the propulsive thrust vector. Also, α and β are the angles of attack and sideslip, respectively, of the mean axis relative to the wind vector.

The virtual work done by the aerodynamic and propulsive forces and moments can now be written as

$$\partial W = \boldsymbol{X}\partial x + \boldsymbol{Y}\partial y + \boldsymbol{Z}\partial z + [\boldsymbol{L} + (y\boldsymbol{Z} - z\boldsymbol{Y})]\partial\phi_B + [\boldsymbol{M} + (z\boldsymbol{X} - x\boldsymbol{Z})]\partial\theta_B + [\boldsymbol{N} + (x\boldsymbol{Y} - y\boldsymbol{X})]\partial\Psi_B + \int_{\text{Area}} \boldsymbol{P}(x, y, z) \cdot \sum \phi_i \partial\eta_i \, \mathrm{d}S$$

Then $Q_x = \boldsymbol{X}$, $Q_y = \boldsymbol{Y}$, and $Q_z = \boldsymbol{Z}$, and $Q_{\phi_B} = \boldsymbol{L}$, $Q_{\theta_B} = \boldsymbol{M}$, and $Q_{\psi_B} = \boldsymbol{N}$. Furthermore,

$$Q_{\eta_i} = \int_{\text{Area}} \boldsymbol{P}(x, y, z) \cdot \phi_i(x, y, z) \, \mathrm{d}S$$

and the development of the vehicle's equations of motion is complete. The resulting state vector may be taken as

$$\text{state vector} = [U, V, W, p, q, r, \eta_1, \eta_2, \ldots, \dot{\eta}_1, \dot{\eta}_2, \ldots]^T$$

Of course, actuation and sensor dynamics may be appended as necessary, utilizing Eq. (1) to include elastic displacements.

Force and Moment Modeling

Consider the issue of modeling the forces and moments. These forces and moments may be expressed in the form to be given, as shown in Ref. 5. The lift L, for example, may be expressed as

$$L = \tfrac{1}{2}\rho_{\text{atm}}\,\text{vel}^2 S_{\text{ref}}\left(C_{L_{\text{rigid}}} + C_{L_{\text{flex}}}\right)$$

where ρ_{atm} is the atmospheric density, S_{ref} the aerodynamic reference area, and vel the velocity of the vehicle c.m. with respect to the atmosphere.

Now the rigid-body lift coefficient $C_{L_{\text{rigid}}}$ may be obtained any way that data would be obtained for a normal simulation. For example,

$$C_{L_{\text{rigid}}} = C_{L_0} + C_{L_\alpha}\alpha + C_{L_\delta}\delta + (\boldsymbol{c}/2\text{vel})\left(C_{L_q} q + C_{L_{\dot{\alpha}}}\dot{\alpha}\right)$$

where δ is the deflection of the horizontal control surface. The coefficients in this expression correspond to the aerodynamic coefficients for the rigid vehicle in its undeformed shape, or jig shape.

The new data that must be generated are the coefficients $C_{L_{\text{flex}}}$, where, for example,

$$C_{L_{\text{flex}}} = \sum_{i=1}^{n}\left\{C_{L_{\eta_i}}\eta_i + \frac{\boldsymbol{c}}{2\text{vel}}\left(C_{L_{\dot{\eta}_i}}\dot{\eta}_i\right)\right\}$$

The aeroelastic coefficients $C_{L_{\eta_i}}$ and $C_{L_{\dot{\eta}_i}}$ may be obtained from an aeroelastic modeling code or, for preliminary analysis, from analytical expressions as developed in Ref. 5. These coefficients capture the effects of elastic deformation, both static and dynamic, on the lift.

Finally, analogous expressions can be developed for the drag D, side force S, and moments, for example, $\boldsymbol{M}$. The key point is that the effects of elastic deflections on the aeroforces and moments are captured through terms such as $C_{L_{\text{flex}}}$.

In addition, the generalized forces Q_{η_i} exciting the elastic DOF (the η_i) must also be developed. These generalized forces may also be expressed in terms of nondimensional coefficients similar to

$$Q_{\eta_j} = \tfrac{1}{2}\rho_{\text{atm}}\,\text{vel}^2 S_{\text{ref}}\left\{C^{\eta_j}_{\text{rigid}} + C^{\eta_j}_{\text{flex}}\right\}$$

where, for example,

$$C^{\eta_j}_{\text{rigid}} = C^{\eta_j}_0 + C^{\eta_j}_\alpha\alpha + C^{\eta_j}_\beta\beta + C^{\eta_j}_\delta\delta + (\boldsymbol{c}/2\text{vel})\left(C^{\eta_j}_p p + C^{\eta_j}_q q + C^{\eta_j}_r r\right)$$

and

$$C^{\eta_j}_{\text{flex}} = \sum_{i=1}^{n}\left\{C^{\eta_j}_{\eta_i}\eta_i + \frac{\boldsymbol{c}}{2\text{vel}}C^{\eta_j}_{\dot{\eta}_i}\dot{\eta}_i\right\} \tag{4}$$

Note now that the effects of the rigid-body motion, for example, α and q, on the elastic deformations $\phi_i\eta_i$ are captured through the preceding generalized forces. Further, the effects of elastic deformation of mode i on the elastic deformations of mode j are also captured in the generalized forces. In other words, the preceding coefficients couple α, q, and so on, to the elastic DOF and couple elastic DOF i with DOF j. All of the preceding coefficients may also be obtained from an aeroelastic code or expressions such as those in Ref. 5.

Case Study 1

Consider a generic, large, swept-wing, high-speed aircraft with a conventional empanage, with descriptive data given in Table 2. The analysis herein will focus on the longitudinal dynamics, although the simulation study addressed both axes. All of the longitudinal aerodynamic and aeroelastic coefficients for the vehicle are listed in Table 3, taken from Ref. 5. The first four symmetric vibration modes of the structure are included in the mathematical model. The mode shapes, given in Ref. 5, indicate that these modes are fuselage- and wing-bending modes.

A time history of the pitch-rate response at the cockpit to elevator input for this generic vehicle is shown in Fig. 1. Also shown in Fig. 1 is the same response if the vehicle were modeled as a

Table 2 Geometry, mass, and inertia of vehicle: case 1

Parameter	Value
Vehicle geometry	
Mean wing chord c, ft	15.3
Wing span b, ft	70.0
Wing planform area S_{ref}, ft^2	1,946
Wing sweep angle Λ, deg	65
Weight W, lb	288,017
Inertia, slug-ft^2	
I_{xx}	950,000
I_{yy}	6,400,000
I_{zz}	7,100,000
I_{xz}	−52,700
$I_{xy} = I_{yz}$	0
Modal generalized masses, slug-ft^2	
M_1	183.6
M_2	9,586.5
M_3	1,334.4
M_4	43,596.9
Modal vibration frequencies, rad/s	
ω_1	12.6
ω_2	14.1
ω_3	21.2
ω_4	22.1
Modal dampings ζ_i	0.02, i = 1, 2, 3, 4

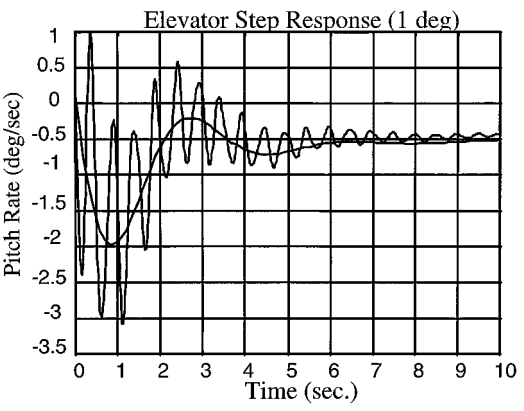

Fig. 1 Attitude-rate time response: flexible vehicle, and rigid vehicle.

Table 3 Longitudinal coefficients for vehicle: case 1[a]

Q_x		Q_z		Q_{θ_B}		Q_{η_i}	$i=1$	$i=2$	$i=3$	$i=4$
C_{X_0}	−0.028	C_{Z_0}	−0.34	C_{M_0}	−0.252	$C_0^{\eta_i}$	0.0	0.0	0.0	0.0
C_{X_α}	0.0035	C_{Z_α}	−0.051	C_{M_α}	−0.029	$C_\alpha^{\eta_i}$	−2.6e−04	4.5e−04	2.6e−04	5.84e−07
$C_{X_{\dot\alpha}}$	0.0	$C_{Z_{\dot\alpha}}$	0.0	$C_{M_{\dot\alpha}}$	−4.3	$C_{\dot\alpha}^{\eta_i}$	0.0	0.0	0.0	0.0
C_{X_q}	−1.7	C_{Z_q}	14.7	C_{M_q}	−34.75	$C_q^{\eta_i}$	−9.49e−02	1.16e−02	3.97e−02	2.83e−05
C_{X_δ}	0.0027	C_{Z_δ}	−0.0076	C_{M_δ}	−0.045	$C_\delta^{\eta_i}$	−2.24e−04	−1.12e−03	4.46e−04	2.56e−06
$C_{X_{\eta_1}}$	0.0	$C_{Z_{\eta_1}}$	−0.0288	$C_{M_{\eta_1}}$	−0.0321	$C_{\eta_1}^{\eta_i}$	5.85e−05	4.21e−03	2.91e−04	2.21e−05
$C_{X_{\eta_2}}$	0.0	$C_{Z_{\eta_2}}$	0.306	$C_{M_{\eta_2}}$	−0.025	$C_{\eta_2}^{\eta_i}$	−9.0e−05	−9.22e−02	1.44e−03	−1.32e−04
$C_{X_{\eta_3}}$	0.0	$C_{Z_{\eta_3}}$	0.0148	$C_{M_{\eta_3}}$	0.0414	$C_{\eta_3}^{\eta_i}$	3.55e−04	1.97e−03	−3.46e−04	9.68e−06
$C_{X_{\eta_4}}$	0.0	$C_{Z_{\eta_4}}$	−0.0140	$C_{M_{\eta_4}}$	−0.0183	$C_{\eta_4}^{\eta_i}$	1.20e−04	3.37e−03	1.44e−04	1.77e−03
$C_{X_{\dot\eta_1}}$	0.0	$C_{Z_{\dot\eta_1}}$	−0.0848	$C_{M_{\dot\eta_1}}$	−0.159	$C_{\dot\eta_1}^{\eta_i}$	−4.20e−04	8.71e−03	−6.29e−04	5.55e−05
$C_{X_{\dot\eta_2}}$	0.0	$C_{Z_{\dot\eta_2}}$	1.03	$C_{M_{\dot\eta_2}}$	1.23	$C_{\dot\eta_2}^{\eta_i}$	−1.97e−04	−2.98e−01	1.95e−02	4.09e−04
$C_{X_{\dot\eta_3}}$	0.0	$C_{Z_{\dot\eta_3}}$	0.0608	$C_{M_{\dot\eta_3}}$	0.172	$C_{\dot\eta_3}^{\eta_i}$	6.50e−04	4.19e−03	−8.77e−06	−4.66e−05
$C_{X_{\dot\eta_4}}$	0.0	$C_{Z_{\dot\eta_4}}$	−0.0199	$C_{M_{\dot\eta_4}}$	−0.0496	$C_{\dot\eta_4}^{\eta_i}$	−1.40e−04	4.15e−03	−1.31e−03	7.99e−02

[a]Units for α and δ deg, q and $\dot\alpha$ rad/s, η_i dimensionless, and $\dot\eta_i$ 1/s.

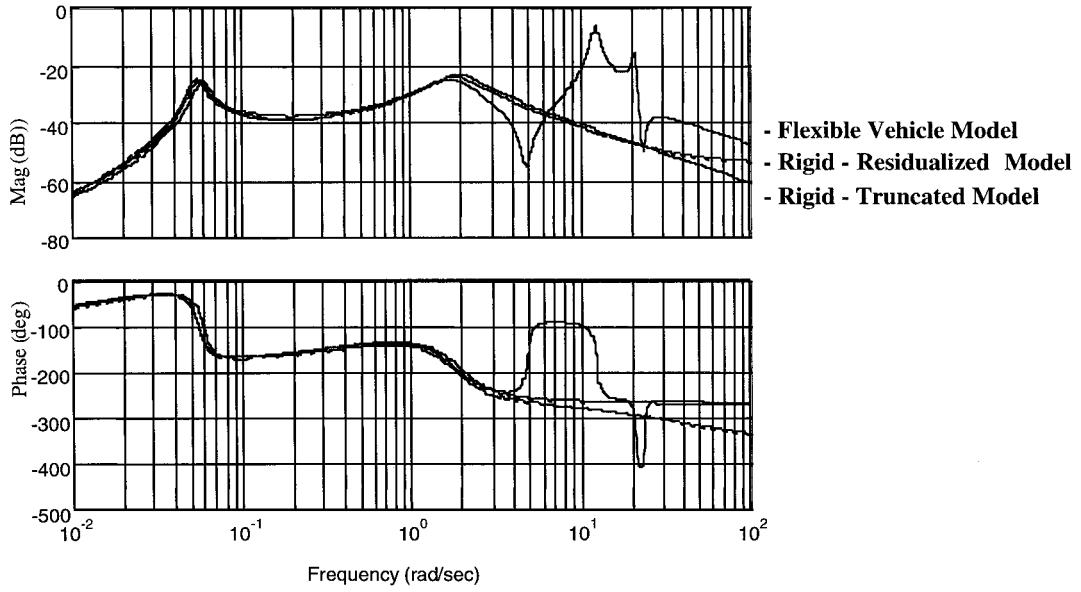

Fig. 2 Pitch rate to elevator frequency response.

rigid body. Clearly the elastic contribution to this response is significant. Similarly, the pitch rate to elevator frequency responses (rad/s/deg) for the elastic- and (two similar) rigid-vehicle models are shown in Fig. 2. Note that the short-period modal frequency near 2 rad/s and the first aeroelastic modal frequency near 2 Hz are evident.

The simulation study in this case used a precision-tracking task, with artificially generated commands displayed on a heads-up display. This task was flown multiple times by several test pilots in NASA Langley Research Center's visual–motion simulator.[6] One of the important experimental variables was the in vacuo vibration frequency of the first symetric fuselage mode, ω_1, a parameter in the dynamic model. Of interest was the effect of this modal frequency on the handling characteristics, with everything else (task, all other parameters in the dynamic model) held constant.

The results from this experiment are presented in Fig. 3, in which the degradation in handling qualities as only the first elastic modal frequency is reduced is clearly evident. The handling qualities of the vehicle if it was purely rigid (all elastic deformations held at zero in the simulation) were rated level 1, whereas the handling characteristics of the baseline vehicle (with lowest frequency of 2 Hz) were rated about 4.5 Cooper–Harper, or level 2. Finally, the handling characteristics degraded to almost level 3, or 7.0 Cooper–Harper, when the lowest elastic mode frequency was reduced to 1.4 Hz.

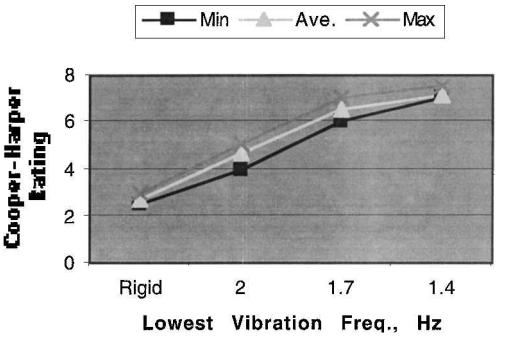

Fig. 3 Effect of increased flexibility on handling characteristics (CHR).

Case Study 2

A second dynamic-aeroelastic simulation model developed as described earlier was more recently implemented in NASA Langley Research Center's visual–motion simulator.[6] In developing the model for this case study, all aeroelastic coefficients [e.g., as in Eqs. (4) and (5)] were estimated via an aeroelastic modeling code. The vehicle in this case was an even larger high-speed aircraft, with weight at the study flight condition around 300,000 lb and length of over 250 ft. The wing was a double delta, and the lowest vibration frequencies were around 1 Hz. The three lowest frequency modes in each axis were modeled, for a total of six elastic modes.

Six test pilots were asked to compare maneuvers performed with and without aeroelastic dynamic effects (ASE) present in the real-time simulation model. The pilots' Cooper–Harper ratings (CHR) of a lateral-offset landing maneuver are shown in Table 4. The offset landing task is a challenging maneuver that requires the pilot to

aggressively correct for a 300-ft lateral offset from the runway centerline at an altitude of 250 ft. Results indicate that the presence of dynamic aeroelastic effects in the simulation model greatly degraded the aircraft flying qualities, particularly in the lateral axis in this task. In some cases pilots changed their lateral/directional CHR from level 1 to level 3 ratings as a result of the aeroelastic effects.

Pilot comments indicated that cockpit vibrations due to aeroelasticity degraded the flying qualities ratings for at least two subtly different reasons. The first is that the vibration environment simply had a negative impact on the comfort level or ride quality at the pilot station. Therefore, pilots increased CHR because the extreme vibrations tended to increase their perception of workload.

Pilots also remarked that cockpit vibrations tended to influence the precision of their control inputs. Some pilots indicated that the vibrations actually resulted in involuntary control inputs. This aeroelastic effect is referred to as biodynamic feedthrough, as noted in Ref. 7. In some cases, the combination of the aeroelastic aircraft, the control stick, and the pilot's biomechanical dynamics may result in a closed-loop system that is unstable or lightly damped. In such instances, cockpit vibrations may cause resonance of the pilot's biodynamic frame, resulting in sustained feedthru of aeroelastic vibrations back into the control stick, a condition referred to as biodynamic coupling. An analytical model of a similar coupling phenomenon was presented in Ref. 8, based on the analysis of flight data.

Figure 4 presents an analysis of a lateral-offset landing task in which the pilot experienced biodynamic coupling while flying the aeroelastic configuration. Frequency and time data shown in Fig. 4 have been normalized as follows: f_0 is normalization frequency, corresponding to peak in voluntary pilot input frequency spectrum obtained from power spectral density (PSD) of pilot stick time histories, and T_0 is normalization time step, $1/f_0$.

Table 4 Impact of aeroelastic effects on CRH: case 2

	Pilot					
ASE	A	B	C	D	E	F
Longitudinal CHRs						
Off	3	4	4	5	4	5
On	6	7	6	7	5	6
Lateral/directional CHRs						
Off	3	3	3	4	4	5
On	4	7	8	6	5	7

The time history at the top of Fig. 4 shows lateral cockpit accelerations in g (dashed line) and lateral stick deflections (solid line). Although the units on the two quantities differ, the scaling of ± 1 is convenient because it represents the maximum normalized throw for lateral stick deflection and because lateral acceleration commanded by the simulation remained in the range of ± 1 g. The plot in the lower left of Fig. 4 shows the PSD of lateral accelerations and lateral stick deflections applied to a segment of the time history. The frequency spectrum of the pilot's control inputs during this period lies within the pilot's voluntary input bandwidth. The frequency spectrum of the lateral accelerations at the pilot station shows some content at the first and second antisymmetric mode frequencies due to minor turbulence excitation of these structural modes.

The power spectrum of a later segment of the time history is shown in the lower middle of Fig. 4. This plot indicates that the bulk of the pilot's input spectrum remains in the voluntary frequency band, but it also shows some frequency content of the pilot's inputs in the range of the lateral elastic modes. Once the pilot begins to move the stick at the resonant frequency of the first antisymmetric structural mode, there is tremendous potential for the lateral mode to be excited by the control inputs, producing larger lateral accelerations at the pilot station. These lateral accelerations move the pilot's frame in a fashion that produces involuntary control inputs that further excite the structural mode. The third power spectrum plot at the lower right of Fig. 4 covers the final segment of the time history. Here, the spectrum of the pilot's stick input exhibits a pronounced resonant peak at the frequency of the first antisymmetric structural mode. It is highly unlikely that the pilot's inputs in this frequency range are voluntary. Video of the seated pilot clearly showed a correlation between lateral stick inputs and involuntary lateral motions of the pilot's upper body. A clear change in the character of the pilot's stick inputs is apparent in the time history, indicating well-developed biodynamic coupling as lateral accelerations feed through the pilot's

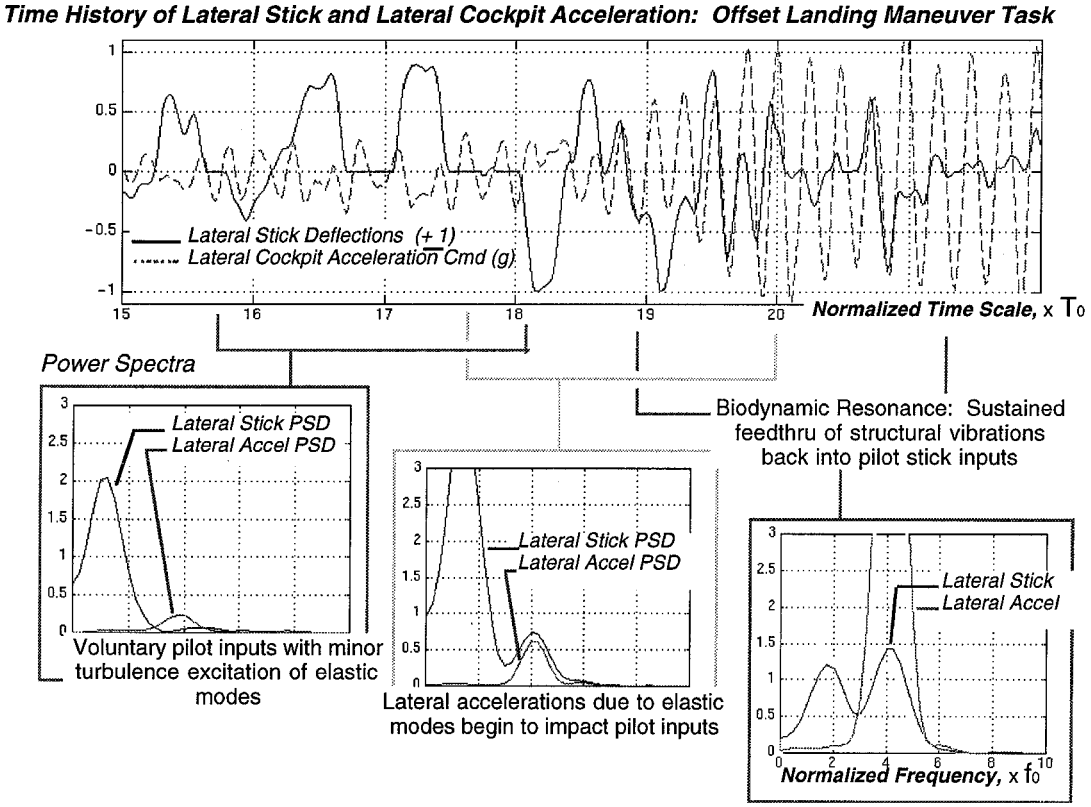

Fig. 4 Example of biodynamic coupling incident.

frame and back into the control inceptor. The pilot could break the involuntary coupling loop if the stick was released, but the flare is being appproached, and, therefore, the pilot is unwilling to do so.

A number of similar incidents of biodynamic coupling were encountered when test pilots flew the aircraft model with structural modes present in the simulation. Encounters with biodynamic coupling were always dangerous and sometimes catastrophic. At least three of the six test pilots encountered biodynamic coupling during some portion of the experiment. Examples of such incidents for pilots B, E, and C are shown in the Fig. 5. Power spectra of the pilots' stick inputs for each of these cases indicate a resonant peak at the frequency of the first antisymmetric elastic mode. Also indicated in Fig. 5 are the pilots' CHR, the ride-quality ratings (RQR), and control-influence ratings (CIR) for each test. Descriptions of the RQR and CIR scales are shown in Table 5.

By contrast, very little biodynamic coupling was excited by the symmetric elastic modes in the longitudinal axis. The lateral axis is far more prone to such coupling for a number of reasons. First, the pilot's seat tends to support the body longitudinally and vertically, but not laterally, so side-to-side accelerations are more difficult to resist. Furthermore, symmetric modes produce vertical accelerations, while the stick input is fore and aft, and so there is less tendency for the pilot's body motions to feed directly into the stick. However, antisymmetric modes produce lateral accelerations that feed directly into lateral stick deflections. A sidestick control inceptor was used in this experiment. The susceptibility of various inceptor types to biodynamic feedthru is a potential topic for future investigations.

To summarize, biodynamic coupling is indicated when cockpit vibrations due to elastic modes feed directly through the pilot's arm and back into the control stick, creating a lightly damped or unstable closed-loop system. The phenomenon is evidenced by a resonant peak in the power spectrum of the pilot's stick inputs at the frequency of one or more of the dynamic elastic modes. The tendency to couple with structural modes appears to increase when pilots tighten their grip on the stick, often in preparation for the flare as the aircraft nears the runway. The phenomenon is influenced by design of the control inceptor and control laws, piloting style, and probably even various aspects of the pilot's physical stature. These results highlight the importance of modeling and simulation of aeroelastic effects when assessing the flight dynamics and flying qualities of large flexible aircraft.

Demands on the Simulation Facility

Figure 6 is from a 1973 report that documented the frequency-response capabilities of the NASA Langley Research Center visual–motion simulation facility.[6] The input/output amplitude ratios for vertical and lateral sinusoidal inputs of 1.8 in. are shown, along with the resulting phase lag, for input frequencies from 0.1 to 12 rad/s. Also shown in Fig. 6 is the frequency range of the dynamic elastic modes that were included in the simulation experiments described

Table 5 ASE influence rating scales

Influence on pilot's control inputs	CIR	Assesment	Influence on ride quality	RQR	Assesment
Pilot does not alter control inputs as a result of aircraft flexibility	1	Acceptable[a]	Cockpit vibrations do not impact ride quality	1	Acceptable[a]
Pilot intentionally modifies control inputs to avoid excitation of flexible modes	2	Marginal[b]	Cockpit vibrations are perceptible but not objectionable	2	Acceptable[a]
Cockpit vibrations impact precision of voluntary control inputs	3	Unacceptable[c]	Cockpit vibrations are mildly objectionable	3	Marginal[b]
Cockpit vibrations cause occasional involuntary control inputs	4	Unacceptable[c]	Cockpit vibrations are moderately objectionable	4	Marginal[b]
Cockpit vibrations cause frequent involuntary control inputs	5	Unacceptable[c]	Cockpit vibrations are highly objectionable	5	Unacceptable[c]
Cockpit vibrations cause sustained involuntary control inputs or loss of control	6	Unacceptable[c]	Cockpit vibrations cause abandonment of task	6	Unacceptable[c]

[a]No improvement necessary. [b]Improvement desired/warranted. [c]Improvement required/mandatory.

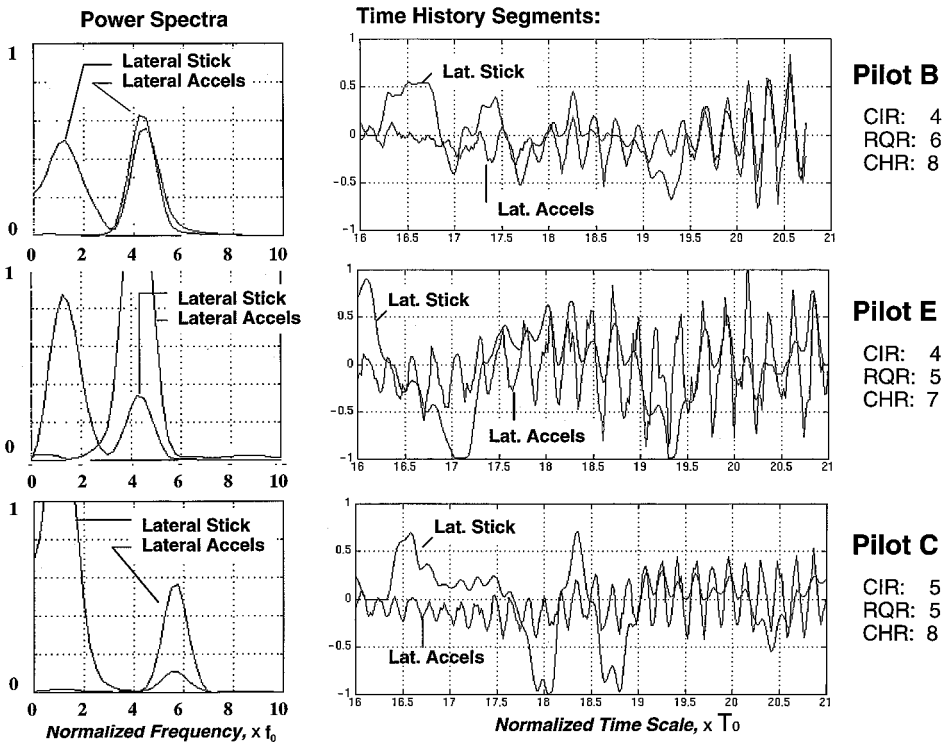

Fig. 5 Biodynamic coupling incidents for 3 pilots.

earlier. It is clear that the dynamic elastic portions of the model reside at the upper threshold of the motion platform's capabilities. The motion base appears to possess reasonable performance at the lowest elastic mode frequency range indicated in Fig. 6 (0.8 amplitude ratio vertically and 1.0 amplitude ratio laterally, with about 15 deg of phase loss).

Figure 7 provides a comparison of vertical accelerations at the pilot station that were commanded by the real-time simulation (dashed line) with those that were actually produced by the motion platform as measured by accelerometers (solid line). The time history was taken from a landing task that was performed with dynamic aeroelastic effects present in the model in which the pilot experienced biodynamic coupling. The plot at the top of Fig. 7 shows that the magnitude of the two signals compared favorably, with the motion platform sometimes delivering vertical acceleration cues as high as 0.4 and 0.6 g. The two segments at the bottom of Fig. 7 provide a closer look at the frequency content, amplitude ratio, and time delay between the two signals. The frequency content of the signals generally appears similar, although a time delay is apparent between the command and the actual measured acceleration. This delay is approximately equal to $0.06 \times T_0$. The accelerometer measurements, shown in the small-amplitude excerpt at the bottom left of Fig. 7, appear to contain an uncommanded high-frequency component at many of the inflection points in the time history. The cause of this small-amplitude aberration is uncertain, but it is most likely due to mechanical slop in the structural components of the motion platform or the mounting of the accelerometer package itself. This vibration is present throughout the time history, but its magnitude is small in comparison to the commanded accelerations.

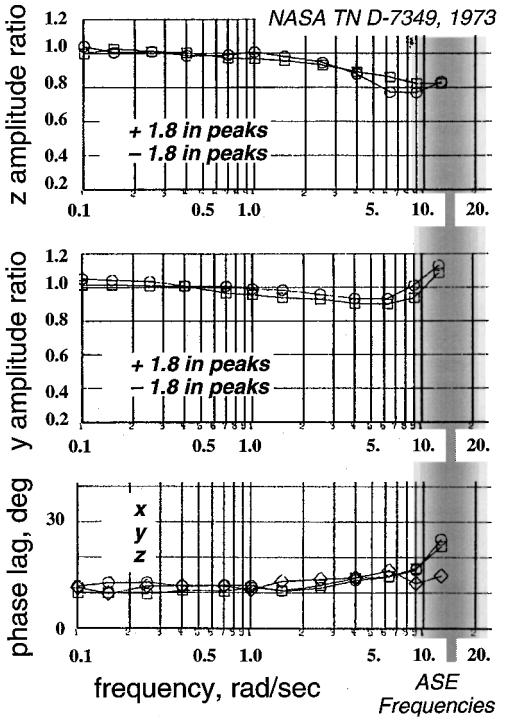

Fig. 6 Frequency response of NASA Langley Research Center visual–motion simulator.

Figure 8 provides a comparison of lateral accelerations at the pilot station that were commanded by the real-time simulation (dashed line) with those that were actually produced by the motion platform as measured by accelerometers (solid line). The comparison of the lateral accelerations appears similar to the earlier comparison of the vertical acceleration. The two segments at the bottom of Fig. 8 provide a closer look at the frequency content and time delay between the two signals. A time delay is apparent between the commanded and measured accelerations, which is slightly longer than that observed in the vertical axis. The accelerometer measurements shown in the small-amplitude excerpt at the bottom left of Fig. 8 again contain an uncommanded high-frequency component at many of the inflection points in the time history. The amplitude ratio between the actual and commanded lateral accelerations is approximately 0.8. The extent to which these motion fidelity limitations impacted the assessment of dynamic aeroelastic effects is thought to be minimal, but their presence should be kept in mind when interpreting the results of the simulation.

The measured accelerations of the simulator cab indicate that the motion base provided a reasonable representation of the dynamic aeroelastic model in terms of frequency content and magnitude of the motion cues. As aircraft designs become larger and more flexible, the need for improved motion-based simulation facilities capable of accurately representing elastic effects increases in significance.

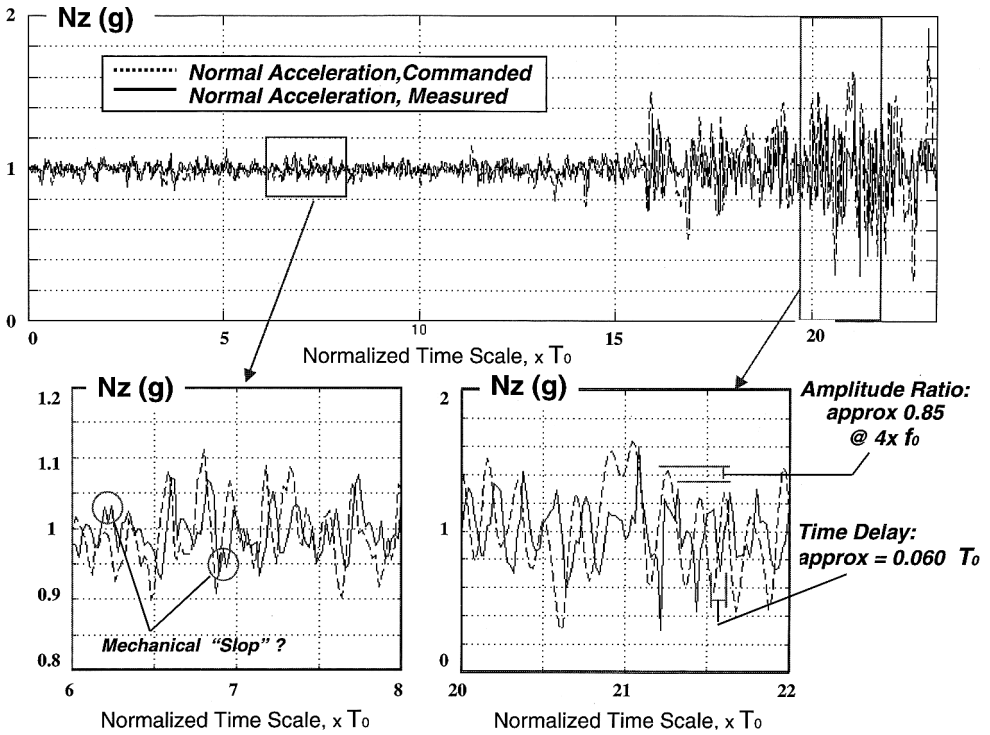

Fig. 7 Motion platform reponse: Nz at pilot station.

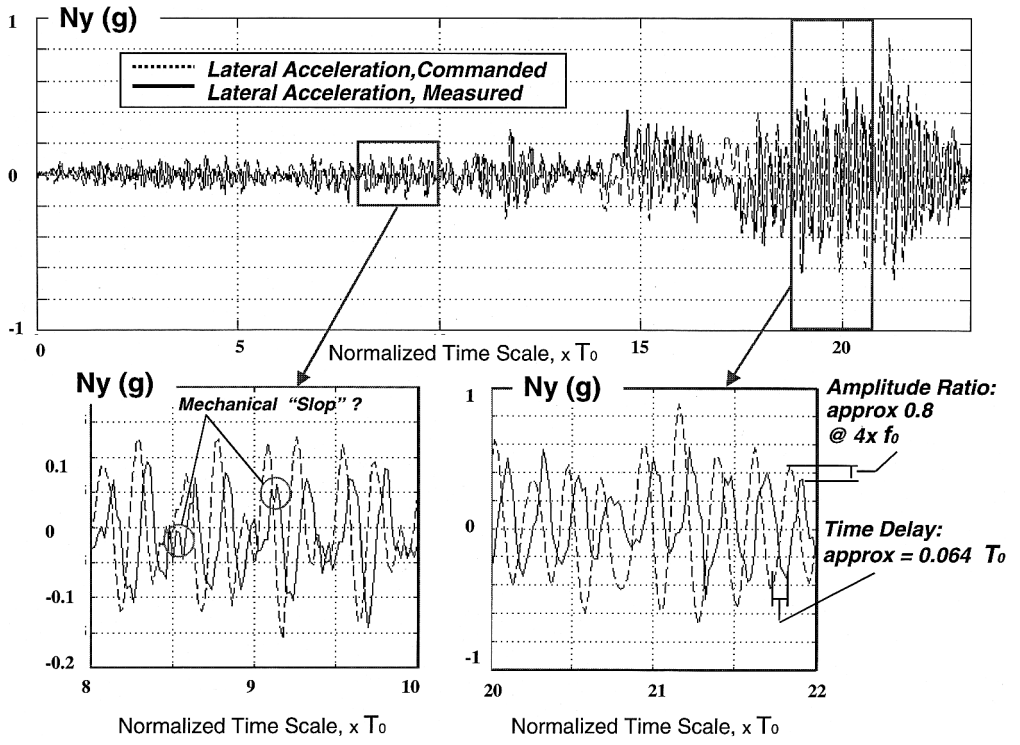

Fig. 8 Motion platform reponse: *Ny* at pilot station.

Conclusions

The focus was on the need for accurate modeling and high-fidelity simulation of highly flexible aircraft, and an appropriate modeling technique was presented. This technique allows for elastic DOF to be added to an existing simulation model of a rigid vehicle. Experimental results obtained from two motion-based piloted simulations of generic high-speed aircraft clearly demonstrated the significant impact that dynamic aeroelasticity can have on the flying qualities of such vehicles. The simulations also revealed the potential for a dangerous form of dynamic interaction referred to as biodynamic coupling. The results highlight the need for motion-based simulation facilities capable of accurately representing elastic effects so that the flight-dynamic and flying-qualities characteristics of such aircraft may be more clearly understood.

Acknowledgments

The first author thanks Sang Lee for generating a significant portion of the numerical results presented. Both authors express thanks to the associate editor and reviewers, for many helpful comments and suggestions.

References

[1]Waszak, M. R., Davidson, J. D., and Schmidt, D. K., "A Simulation Study of the Flight Dynamics of Elastic Aircraft," Vols. 1 and 2, NASA CR 4102, Dec. 1987.

[2]Schmidt, D. K., "Integrated Control of Flexible High-Speed Aircraft," AIAA Guidance, Navigation, and Control Conf., Baltimore, MD, Aug. 1995.

[3]Newman, B., and Buttrill, C., "Conventional Flight Control for an Aeroelastic, Relaxed Static Stability High-Speed Transport," AIAA Guidance, Navigation, and Control Conf., Baltimore, MD, Aug. 1995.

[4]Milne, R. D., "Dynamics of the Deformable Airplane," Parts 1 and 2, Her Majesty's Stationary Office, Repts. and Memoranda 3345, Sept. 1962.

[5]Waszak, M. R., and Schmidt, D. K., "Flight Dynamics of Aeroelastic Vehicles," *Journal of Aircraft*, Vol. 25, No. 6, 1988.

[6]Parrish, R. V., Dieudonne, J. E., Martin, D. J., and Copeland, J. L., "Compensation Based on Linearized Analysis for a Six-Degree-of-Freedom Motion Simulator," NASA TN D-7349, 1973.

[7]Ashkenas, I. L., Magdaleno, R. E., and McRuer, D. T., "Flight Control and Analysis Methods for Studying Flying and Ride Qualities of Flexible Transport Aircraft," NASA Contractor Rept. 172201, Systems Technology, Contract NAS1-1847, Aug. 1983.

[8]Smith, J. W., and Montgomery, T., "Biomechanically Induced and Controller-Coupled Oscillations Experienced on the F-16XL Aircraft During Rolling Maneuvers," NASA TM 4752, 1996.